NORTHWESTERN UNIVERSITY

System Design and Verification of the Precession Electron Diffraction Technique

A DISSERTATION

SUBMITTED TO THE GRADUATE SCHOOL
IN PARTIAL FULFILLMENT OF THE REQUIREMENTS

for the degree

DOCTOR OF PHILOSOPHY

Field of Materials Science and Engineering

By

Christopher Su-Yan Own

EVANSTON, ILLINOIS

First published on the WWW 01, August 2005

Build 05.12.07. PDF available for download at:
http://www.numis.northwestern.edu/Research/Current/precession.shtml

CHAPTER 5

Precession Examples

In chapter two, a high-performance precession system was built and the parameters for its operation were determined. Chapters 3 and 4 provide a theoretical understanding and experimental basis supporting it. Parameters for good precession experiments have been described. This chapter will demonstrate precession experiments on real specimens using the principles described in the previous chapters. Some of the experiments were conducted before a complete understanding of favorable experimental parameters for PED were known. However, it will be seen that the results are consistent with the analyses previously described.

All TEM samples were prepared by crushing larger polycrystals and dispersing them onto a copper grid supporting holey carbon film. Diffraction experiments were conducted on specimen edges that did not overlap carbon film in order to avoid the superposition of scattering from carbon with the crystal diffraction pattern.

5.1. (Ga,In)$_2$SnO$_4$

Here we revisit the GITO model system a final time. In chapter 3, the atom positions in the 010 projection in GITO were found using two processing methods prior to input into direct methods: 1) high-pass filtered experimental amplitudes and 2) intensities. The rationale for using intensities was explained in section 4.3. Here we will solve the structure using corrected intensities using the two-beam dynamical correction factor C_{2beam} (equation 4.14). While this requires a forward calculation based upon known structure factors, this exercise will illustrate the two-beam model's accuracy, demonstrate the validity of using intensities as an approximation to the two-beam correction experimentally, and reaffirm the data quality from the GITO precession experiment.

The true structure factors based upon the atomic positions from Sinkler et al. (1998b) were used to calculate C_{2beam}-type correction factors using equation 4.14. The experimental cone semi-angle of $\phi =$ 24 mrad, determined by measuring the radius of the beam tilt ring with descan off, and the thickness of 412 Å (determined in section 3.3 using multislice calculations) were used for calculating the correction factor. Figure 5.1(a) shows the correction factor plotted against spatial frequency g. The correction factor was then applied to the experimental intensities from chapter 3 — measured in the PED pattern out to a spatial frequency of 1.4 Å^{-1} — to generate corrected experimental amplitudes (figure 5.1(b)). Recall that the incident radiation energy was 200kV.

At the end of chapter 4, it was shown that in the limit of large structure factor and thickness, the intensities that have been corrected for two-beam dynamical scattering will behave like the square of the structure factor. The caveat was that weaker structure factors might not follow this trend, as will
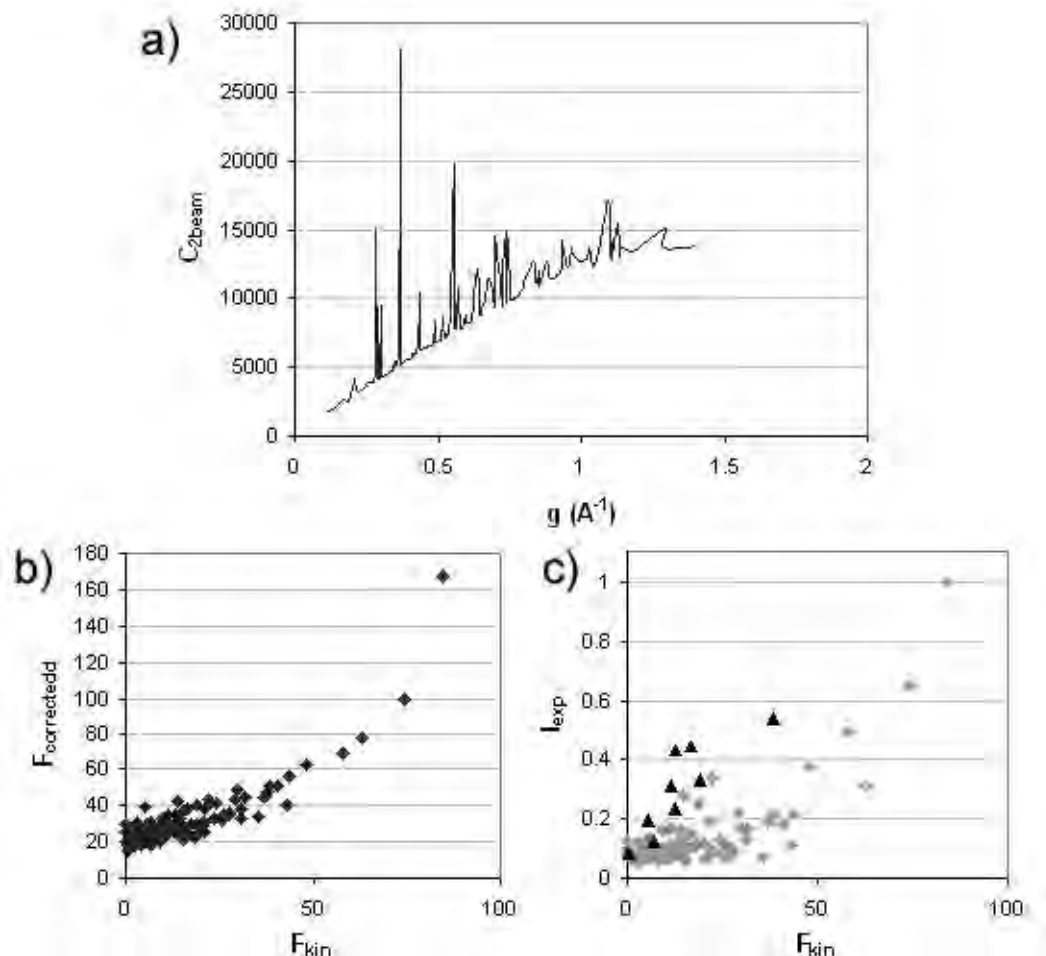
Figure 5.1. (a) C_{2beam} correction factors calculated for GITO using true structure factors and known experimental parameters ϕ =24 mrad and t = 412Å. (b) The experimental amplitudes corrected by C_{2beam} v. true structure factor . (c) Intensities plotted against true structure factor for the GITO system. Black triangles correspond to low-index reflections with $g < 0.25$ Å^{-1}. The grey data points represent reflections in the range from $g = 0.25$-1.4 Å^{-1}.

demonstrated in this example. For reference, the experimental PED intensities from figure 3.4(b) have been plotted against the true structure factors. The grey data points correspond to reflections in the range of $g = 0.25$-1.4 Å^{-1}, and the spatial frequencies that were found by multislice to have high error ($g < 0.25$ Å^{-1}, see section 3.2.2) have been plotted separately using black triangles. Excluding these black triangles that result from multi-beam coupling, there is a striking similarity between the C_{2beam}-corrected amplitudes and the rest of the intensity dataset, demonstrating adherence to equation 4.19. Of these, the reflections that demonstrate large error are the reflections near the transmitted beam (low **g**).

They are amply corrected in figure 5.1(b) showing that they are two-beam in nature — likely the result of systematics — and excluding them would be advantageous in further ensuring dataset linearity.

Referring back to the theoretical result — the plot corresponding to 24 mrad, 48 nm in figure 4.11 — the C_{2beam}-corrected experimental dataset is dissimilar to the theoretical only in that the low-g region should have a larger spread. This can be explained by the fact that missing reflections are likely low-amplitude reflections spread throughout the PED pattern that were below the measurement threshold. The intensities and corrected amplitudes have very similar characteristics in the strong reflections and should generate similar structure maps.

The direct methods solution using the intensities shown in figure 5.1(c) has already been shown in figure 3.6. A new direct methods solution was generated using the corrected amplitudes in figure 5.1(b), and this is shown in figure 5.2. The new solution is essentially identical to the earlier solution using intensities, showing that similar phase relationships were recovered by direct methods for the structural reflections. Some of the structure-defining amplitudes were stronger, giving better-localized peak shapes that are evident in comparing the two maps. The agreement between the datasets in figures 5.1(b) and 5.1(c) and the theoretical reference dataset in 4.11 confirms that the two-beam model is applicable in the thickness regime where a correction factor would be needed. It also demonstrates experimentally that using the intensities is a valid approach as a first (and much-needed) *a priori* approximation to the two-beam correction factor for thick specimens, effectively extending the range of thicknesses that PED can handle.

5.2. $La_4Cu_3MoO_{12}$

The first precession experiment conducted on the 300kV Hitachi UHV H-9000 system was on the $La_4Cu_3MoO_{12}$ materials system (Own et al. 2004). This early experiment showed some promising results even though the experimental conditions were not particularly favorable. To be more specific, the precession cone semi-angle ϕ was only about 20 mrad, the integration was not complete, the specimen was very thick (> 35 nm), and the measurement methods for precession data were not as accurate as in
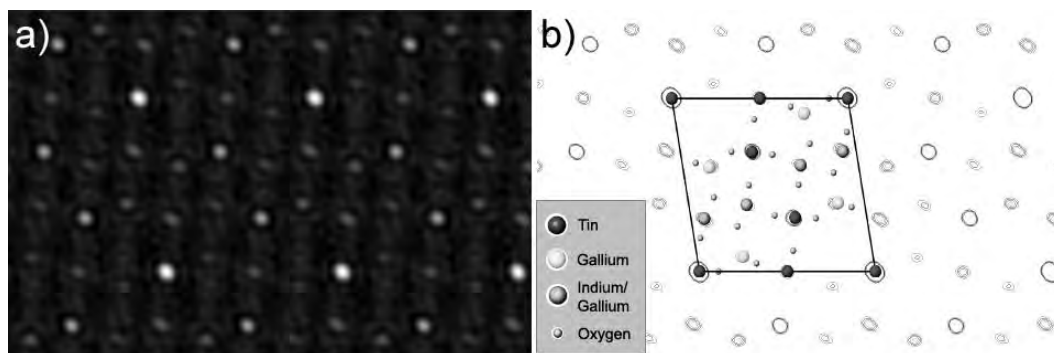

Figure 5.2. (a) Direct methods potential map from amplitudes corrected for 2-beam effects (C_{2beam} correction factors, figure 5.1(b)). (b) Contour map of (a) with the atoms overlaid.

later precession implementations. However, employing the methods developed in this thesis for dealing with thick specimens, useful structural information was extracted from this data.

$La_4Cu_3MoO_{12}$ is a complex oxide exhibiting "frustrated" magnetic behavior. The structure is a homeotype of $YAlO_3$, a rare-earth hexagonal phase. The crystal is very slightly monoclinic but was assumed to have a rectangular cell for the calculations. Unit cell parameters are a = 6.86 Å, b = 10.98 Å, and c = 7.9147 Å, and β = 90.02° (Griend et al. 1999). The structure model in the [001] projection is shown in figure 5.3. Intra-triangle anti-ferromagnetic interactions align two of three spins, yielding trimers with $S_{total} = \frac{1}{2}$. This spin coupling causes an ordering between adjacent cells that doubles the unit cell along the a direction. The space group for this structure is $P112_1/m$, translating into P2gm symmetry in the [001] projection.

During refinement of the X-ray data using ShelX software by Griend et al. (1999), it was found that the structure model derived from X-ray diffraction intensities had much better R-factors (improved by a factor of two, to $\approx$ 5%) if a twinning model was introduced to improve the match with the intensities. Because the data was acquired from a single-crystal X-ray diffraction experiment, the question arises as to what sort of length scale the twinning really occurs at (if it exists at all). Electron microscopy is
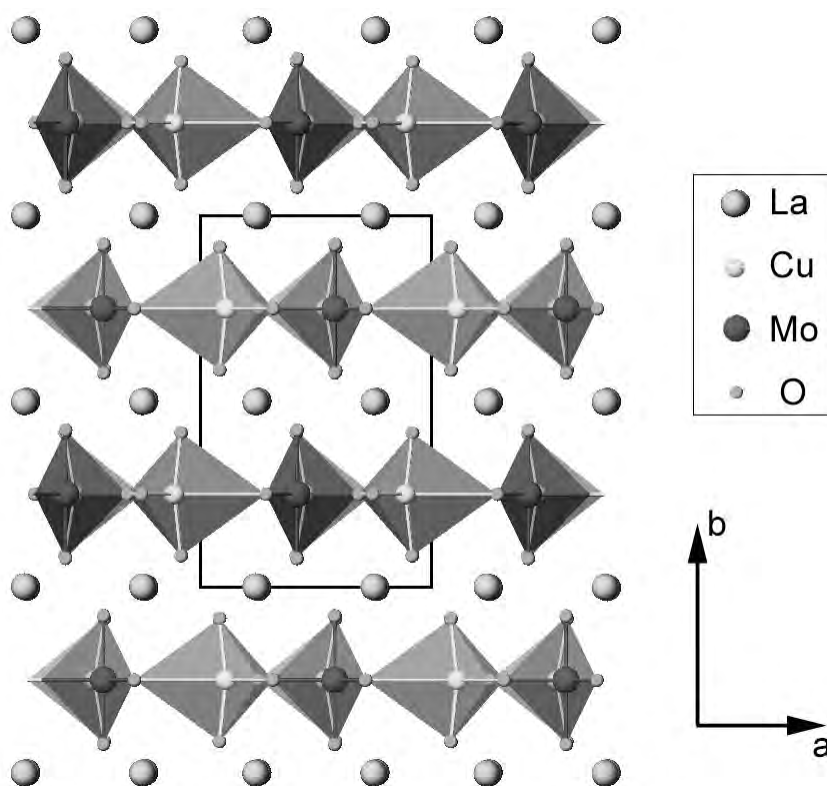

Figure 5.3.   [001] projection of the $La_4Cu_3MoO_{12}$ structure model. In this model, the frustrated structure alternates Mo-rich columns along the b-axis to ensure stoichiometry, resulting in a doubling of the unit cell along a.

a suitable tool for studying this due to its ability to probe single-crystal regions of the specimen at very fine length scales.

Diffraction patterns along the [001] zone axis of a $La_4Cu_3MoO_{12}$ crystal were taken in both selected-area and precession modes ($\approx$ 20mrad precession angle) from a crystal edge in a powder specimen (figure 5.4(a)). Nine negatives comprised each exposure series and were digitized using an Optronics microdensitometer at a scale of 25 μm per pixel. SADP intensities were then acquired by first pattern-matching a unitary spot motif to the digitized diffraction spots and then integrating the intensity of the matched pattern. Precession intensities were quantified in a slightly different way by first applying a background subtraction algorithm within a masked area around each spot and then integrating the remaining intensity. The measurement procedures are discussed in more detail in appendix F.

Reduction of nine data sets into a single set was conducted by scaling the data from each negative while minimizing the overall error between data sets. Details of this procedure can also be found in appendix F. Intensities from the precession exposure series matched very well when scaled, resulting in extremely low error between negatives. Compared to the conventional SAD data set, the precession data set had errors at least an order of magnitude better. This is an important practical point; the lower error can be attributed to the fact that the precession technique is much less sensitive to minor variations in the experimental conditions, and is consequently less susceptible to systematic errors than the SAD
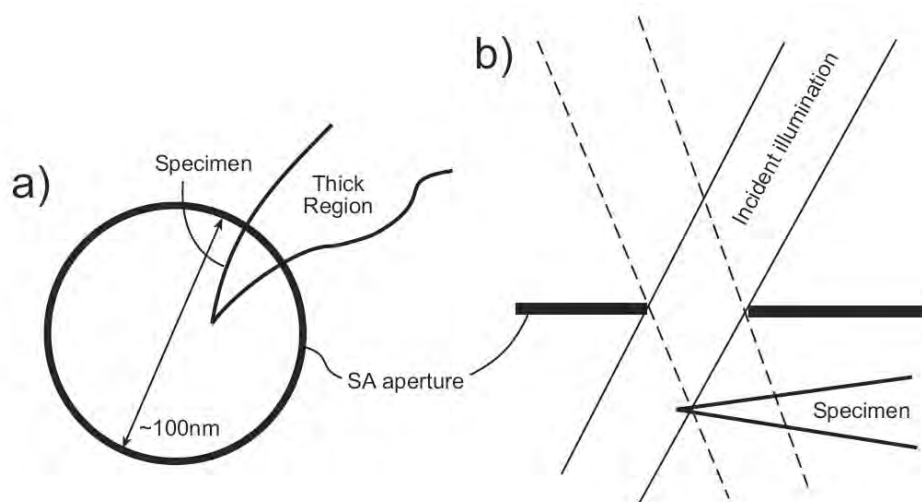

Figure 5.4. Experimental conditions for the $La_4Cu_3MoO_{12}$ precession diffraction experiment. The selected-area image (with precession off) is shown in (a). The specimen morphology was a spike shape with thin region masked using the selected-area aperture. The sample became very thick just outside of the masked region. With precession on, the probe, specimen, and aperture image wander because of optical aberrations and SA errors occurring, for example, if the aperture is not conjugate with the specimen plane. Incomplete integration and/or thickness sampling variation along the circuit may result as shown in (b).

methods. Precession provides nearly the same intensities for symmetry-equivalent reflections and is fairly tolerant of a slightly off-zone diffraction condition.

Figures 5.5(a)-(c) show the kinematical diffraction pattern, the selected-area diffraction pattern (SADP), and PED data set (non-symmetry-averaged). The intensity of each reflection is represented using grayscale as well as spot size to visually demonstrate relative spot intensities. Intensities were collected to ≈ 3 Å^{-1} in the conventional diffraction pattern whereas measureable intensities extended only to about 2.25 Å^{-1} in the precession pattern. This is a common behavior with precession patterns because systematic dynamical scattering is reduced by precession, and in this case the Lorentz geometry decreases sampling limits for the higher-index reflections. Less intensity is scattered out to high-index reflections through dynamical scattering paths, therefore precession patterns will have less intensity at high angle than their conventional diffraction counterparts.

The SADP has the effects of considerable specimen tilt. The precession pattern was acquired from the same illuminated region using the same specimen tilt condition as the SADP, and it is apparent that the Friedel symmetry has been improved considerably. There is a slight emphasis toward one side of the precession pattern (apparent in a slightly larger ($2\bar{1}0$) spot); this can be attributed to the fact that the pattern was taken from a thick wedge-shaped specimen using low precession angle. Thickness effects are considerable with smaller ϕ, as explained in chapter 3, and because of probe wandering, the precession causes the beam to sample different thickness regimes and areas along the circuit. The intensity integrated can thus vary and violate Friedel symmetry even though precession in theory should not. This is uncharacteristic in a well-aligned precession experiment and can be avoided in most cases by ensuring good real space localization during alignment (see appendix E).

The (040)-type reflections in the kinematical pattern are considerably more intense than other reflections. This high intensity is not apparent in the SADP pattern nor in the precessed pattern. There is enhanced dynamical interaction near the transmitted beam as evidenced by the large error occuring for (200)-type reflections. The fine intensity ordering is rather well-preserved in the precessed DP, especially the alternating spots which show, qualitatively, appropriate ratios. The SAD pattern, in contrast, loses some fine information such as the subtle intensity ordering in the reflections that occur between the (130) and ($1\bar{3}0$) spots.

The crystal from which the patterns were taken did not exhibit the superstructure reflections that would otherwise occur as weak spots halfway between strong columns of diffracted spots. The missing superstructure can be explained through two possible mechanisms. If the twinning occurs in every other plane along the b-axis, then the superstructure reflections may disappear. The other possibility is disorder. If the structure is disordered, the distribution of Mo and Cu tetrahedra would be random such that the light grey columns in figure 5.3 would become filled with Mo-rich (darker) tetrahedra.

The measured diffraction intensities were processed for use with direct methods to investigate the twinning model. Three approaches were taken:

(1) Dynamical amplitudes used with direct methods;
(2) Precession amplitudes band-pass filtered and used with direct methods;
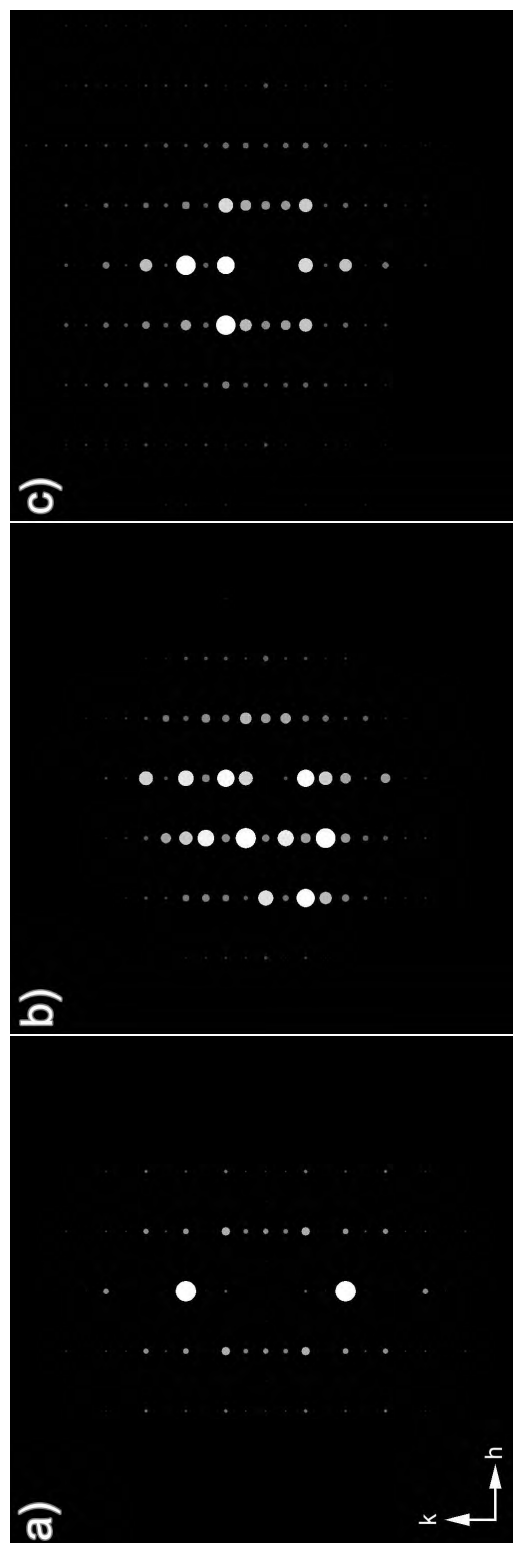(3) Precession intensities band-pass filtered and used with direct methods.

Figure 5.5. La$_4$Cu$_3$MoO$_{12}$ intensity diffraction patterns. (a) Kinematical pattern calculated from the structure in figure 5.3. (b) Conventional on-zone zone-axis pattern (dynamical dataset). The dataset had considerable tilt, so intensities are not symmetric. This was exacerbated by large specimen thickness. (c) Precession pattern from the same specimen region as (b) taken under the same specimen tilt conditions. Precession angle was 20 mrad.

Because the precession angle was not large, the intensities needed to be band-pass filtered to avoid the region past $2R_0$ (where R_0 is the radius of the zeroth order Laue zone). For $\phi = 20$ mrad and 300 kV radiation, reflections beyond 2 Å^{-1} needed to be rejected. The reflections with $g = 0.25$-1.5 Å^{-1} were used with direct methods to ensure ample integration of intensity.

The dynamical amplitudes did not generate sensible structure maps, not a surprising result from bulk diffraction data. Precession amplitudes fared better, however in general the maps had low contrast. The intensities were then used with direct methods to generate structure maps. The quality of the intensities was not ideal and many false solutions were generated in the top solutions, but two families of solutions with distinct sparsely-spaced peak-like features emerged. One family had difficulty localizing the La framework atoms, but the other family gave very realistic cation features. The top amplitude and intensity solutions that gave discrete atom-like features (both 6th ranked) are given in figures 5.6(a)-(b).

One of the difficulties of initially interpreting these structure models was that the Cu/Mo rows had smeared features in many structure maps. It is now recognized that this is possible because of disorder: with partial occupancy of both Cu and Mo tetrahedra in the framework, it would be difficult to precisely localize the Cu and Mo cation columns, which project very closely next to each other. In some maps, it appeared that the oxygen atoms that create the wingtips of the tetrahedra (the oxygen rows between Cu/Mo and La rows) were present. The oxygen atoms — whose positions depend upon which cation they are coordinated with — would likely not be seen in maps if the precession data was of sufficient quality, so peaks appearing at shifted locations that would cause bond angles to deviate too much were
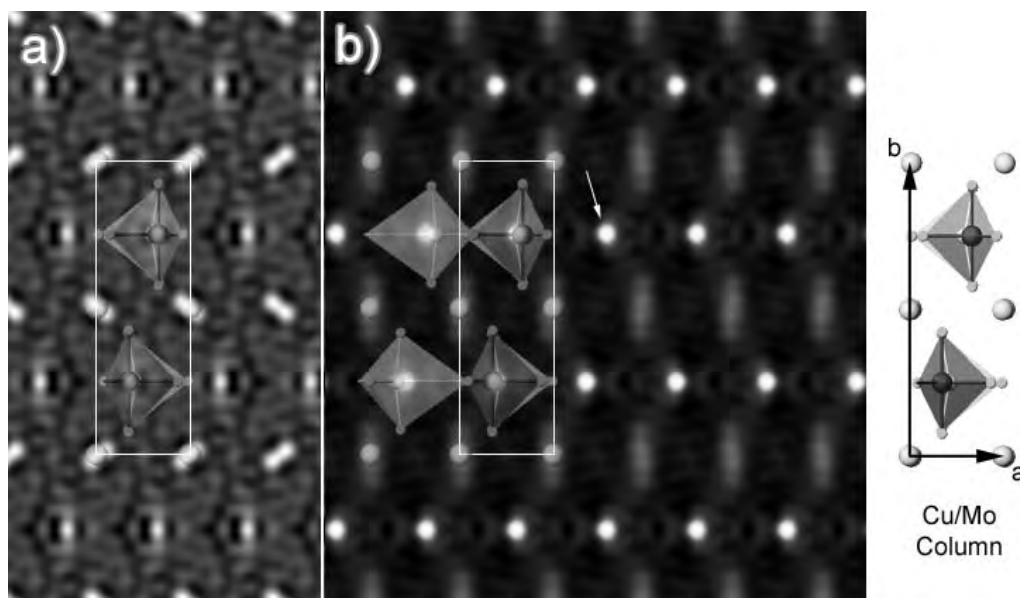

Figure 5.6. Direct methods solutions from PED on La$_4$Cu$_3$MoO$_{12}$. The amplitude solution is shown in (a) and the intensity solution is shown in (b). The frustrated structure suggested in Griend et al. (1999) has been replaced with a disordered structure that includes. The cation positions are localized and show that the mixed Cu/Mo tetrahedra.

considered spurious artifacts. This is also supported by the fact that the oxygen atoms in the Cu/Mo rows are never clearly localized either. This consideration allowed several families of solutions to be eliminated by virtue of false peaks. This left the maps that generated clear atom-like features, but that did not localize the La framework. These were easy to identify and remove, leaving the solution family shown in figure 5.6.

In the new disordered model, the tetrahedral motif is still present. However, the Cu tetrahedra cannot exist in the new structure exclusively within their own columns in the projection plane. In the previous model, the Cu tetrahedra (lighter color) are larger in size in the b-axis, whereas mixed Cu/Mo tetrahedra have a more compressed frame along that axis. Additionally, the location of the Cu cation in the Cu-only column is displaced from the peak location in the map whereas Cu/Mo falls right onto it. This indicates that the average structure contains Cu/Mo tetrahedra dispersed throughout the structure rather than the alternating Cu and Cu/Mo columns. In order to maintain stoichiometry, there must be a consistent ratio between Cu and Mo atoms, nevertheless a random disordered model can still satisfy this constraint. Diffraction is an averaging technique, so the structure maps shown here represent hundreds if not thousands of unit cells. There may be short-range order — which might be identified through nanoprobe precession or high-resolution imaging — however, the superstructure intensities were not seen at all in this crystal, indicating that the disorder is dominant and is widespread throughout the crystal on which the diffraction experiments were conducted.

5.3. Al_2SiO_5

Andalusite (Al_2SiO_5) is an aluminosilicate mineral that crystallizes in a dense orthorhombic cell. This system was used to test the latest precession retrofit on the JEOL 3000F, and was chosen to complement density function theory calculations exploring charge density. Andalusite is orthorhombic with four formula units per unit cell, giving 32 atoms per cell. The cell dimensions are $a = 7.7942$ Å, $b = 7.8985$ Å, and $c = 5.559$ Å with space group Pnnm giving P2 symmetry in the plane.

[$1\bar{1}0$] zone axis patterns were taken from an andalusite powder specimen using conventional diffraction and PED at 300kV. The PED cone semi-angle was 36 mrad. The amplitude diffraction patterns for the two experimental datasets are given in figure 5.7. Figure 5.7(a) shows the conventional DP; the precession pattern, 5.7(b), shows better ordering in the spots. More striking is the absence from the precession pattern of the forbidden reflections of type ($00n$), where n is an odd integer. These reflections — which are quite strong in the conventional pattern — are extinct in the precession pattern, adhering to kinematical behavior.

Amplitudes from both diffraction patterns were each used with direct methods for generating structure maps. All measured reflections were used from the conventional DP while the precessed DP was high-pass filtered to remove $g < 0.25$ Å^{-1}. The top solutions are given in figure 5.8. The structure in this projection has Si and Si/O columns at half the cell distance along each edge flanked by Al columns. The conventional diffraction solution identifies the Si and Si/O positions and the central Al position; it also locates Si/O column positions at the $\frac{1}{2}$-vertical cell location. The conventional diffraction solution does not show all the cation positions but it does hint at the existence of potential around the edges of the unit cell. In contrast, the precession potential map locates all cation positions and also has relatively
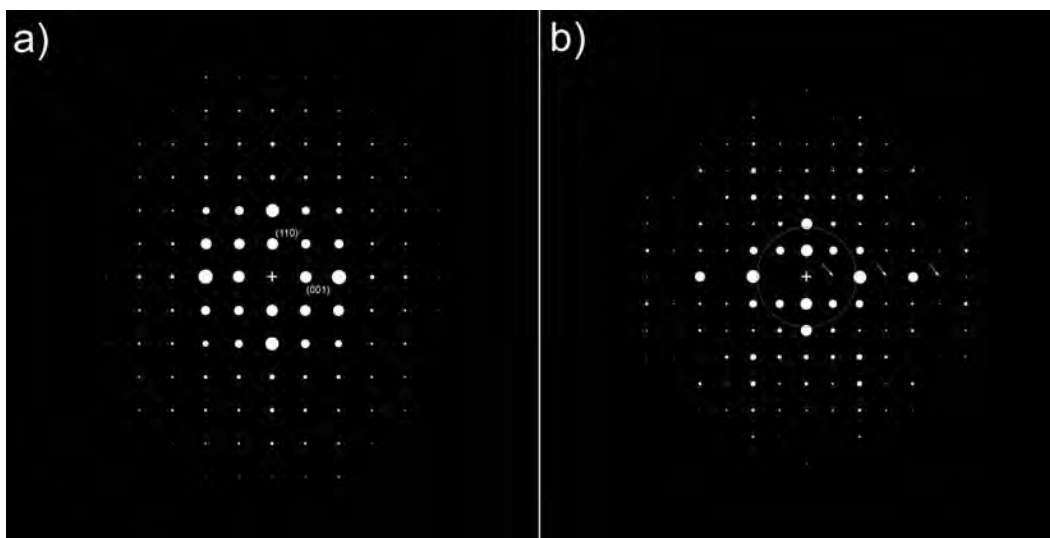
Figure 5.7. Amplitude diffraction patterns from (Al_2SiO_5. (a) Conventional DP and (b) precessed DP ($\phi = 36$ mrad). The amplitude ordering in the precession pattern is more distinct. Additionally, the forbidden reflections (odd-order (001)-type reflections), which are very strong in the conventional pattern, are extinct in the precession pattern as indicated by the arrows. The ring overlay describes the spatial frequency $g = 0.25$ $Å^{-1}$.

good agreement with expected scattering strength. It also indicates some of the vertical peak-splitting that is due to the oxygen atoms projected near the Al atoms on the cell edge. This precession-based solution would be an outstanding *a priori* starting structure from which to conduct refinement.

5.4. Mordenite

Not all structures are amenable to solution by PED. One case is for materials with very large unit cell structures. In studies of unknown structures, the success of the high-pass filtering approach to avoid the low-index errors hinges upon the fact that most structures do not have strong structure factors in the low-g reflections. For structures that are very large — greater than about 12 Å cell size — the slowest-varying spatial frequency in the structure is less than 0.1 $Å^{-1}$.

In section 1.2 it was explained that part of the robustness of the direct methods algorithm used is its ability to interpolate missing reflections. In precession, omitted low-index reflections are also interpolated. For cell structures with considerable scattering strength in the low-index reflections, for example, Mordenite, it may be more detrimental to remove the reflections rather than allowing intensities with large error into the data set. Mordenite is a nanoporous zeolite commonly used as a metal catalyst support. It is very similar to the zeolite ZSM-5, constisting of continuous-pore structures along the [001] direction made up of large 12-member oblong pores of 7 Å × 6.5 Å inner dimension. In addition to being a large cell material, it has a number of characteristics that dramatically reduce its tractability by direct methods:
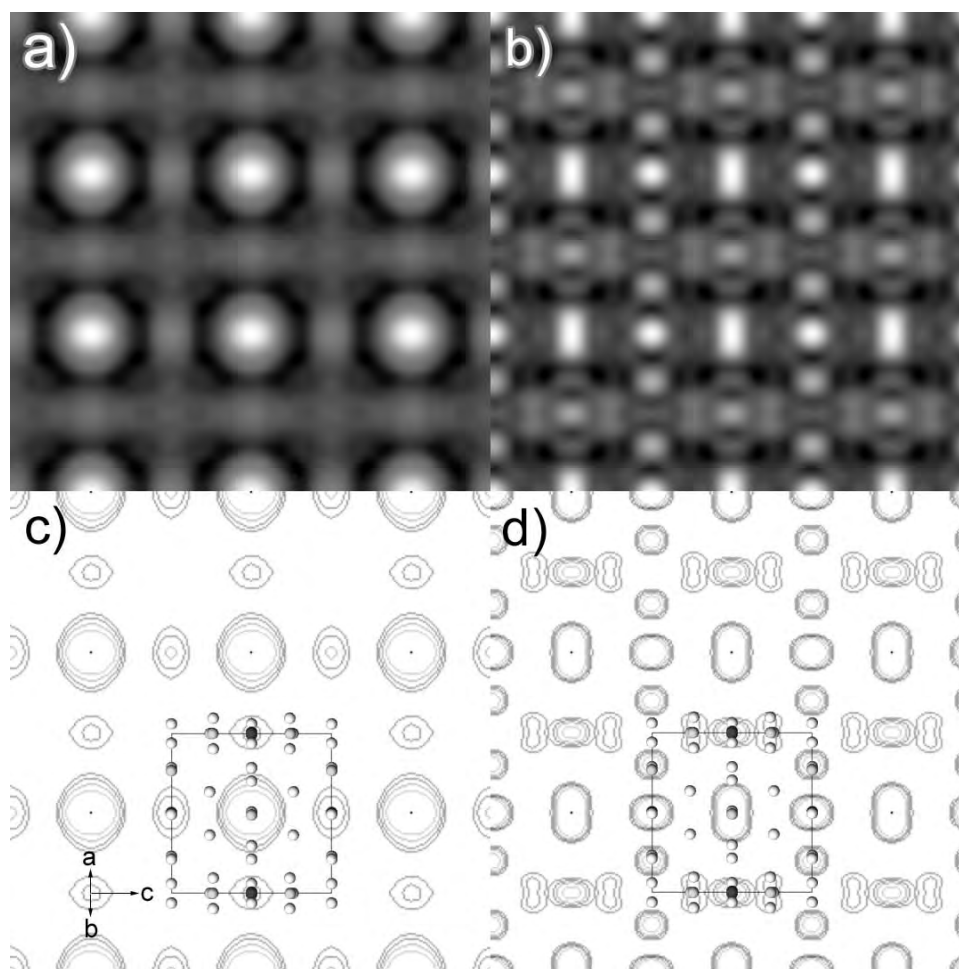
Figure 5.8.   Potential maps from direct methods on Andalusite. (a) Map from conventional amplitudes. (b) Map from high-pass filtered PED amplitudes. Contour plots are shown in (c)-(d) and the structure is overlaid for reference. Dark atoms are Si, light atoms are Al, and white atoms are O. The white atoms along at $\frac{1}{2}$ the vertical distance represent mixed Si/O columns.

(1) The structure projects very poorly, so direct methods will be ineffective unless very accurate structure factors are used;

(2) It is an open-framework structure, so the Debye-Waller temperature factors are enormous ($B_{Si} \approx 1.2$ Åand $B_O \approx 3$ Å).

(3) The cations are both light atoms (Z = 13 and 14), which worsens the above two characteristics.

An experimental mordenite PED pattern was taken at 200 kV on the precession-enabled JEOL 2000FX microscope using a 40 mrad cone semi-angle. The crystal has space group Cmcm, yielding cmm plane group symmetry in the [001] zone with unit cell parameters a = 18.3 Å and b = 20.5 Å. 182 symmetry-equivalent reflections were quantified to a spatial frequency of ≈ 1 Å^{-1}. The intensity

dataset that was acquired on this instrument is shown in figure 5.9(b). The kinematical pattern — calculated using the large temperature factors from above — is shown for reference in figure 5.9(a). A circle describing $g < 0.25$ Å^{-1} is overlaid on top of the experimental pattern demonstrating that many very strong reflections are contained within the regime that is subject to large dynamical error. The resemblance of the precession result to the kinematical intensities, especially the rectangular spot ordering near the transmitted beam, is readily seen. However, the over-emphasis of low-g reflections is also apparent and additionally, the specific ordering and strong intensity of the high-index reflections diminished in the precession pattern.

This type of poorly-projecting structure is generally impossible to solve via direct methods unless very high quality intensities (to high spatial frequency) are provided, or unless known phases from high-resolution images are used to help constrain the direct methods. Direct methods on the kinematical intensities alone will yield the true structure (demonstrated in figure 5.10(a)), however, since there are many overlapping atoms, inclusion of high spatial frequencies is required to pinpoint their locations. Practical experiments only allow measurement to limited spatial frequency, depending upon the dynamic range of the measuring medium, so it is unlikely that precession would be able to recover this structure unless high-resolution phases were available.

At the time of the study, it was not know whether the low index spots contributed considerably to the final structure in the context of direct methods. The beams are very strong, so direct methods was initially conducted using the full set of amplitudes. Surprisingly, only one unique solution resulted from this exercise. This initial map was confusing because it placed a large amount of intensity within the pore centers and exhibited spurious oscillations throughout the denser regions of the structure.

The homologue of mordenite investigated here often has relatively thick platelet morphology of $\approx$ 500 Å, so it was decided that intensities could possibly give better results and direct methods was run a second time using high-pass filtered intensities. The standard high-pass filtering cutoff of 0.25 Å^{-1} was applied to this set, removing a large number of strong reflections. A set of four unique solutions was obtained describing two solution families, one of which exhibited slightly smeared strong features, and the other containing more peak-like features. The second solution family is shown in figure 5.11 (contrast is reversed).

One effect that can occur with direct methods is that the algorithm may consistently converge to a particular configuration of phases. The Babinet solution, which is the inverse of the potential map with opposite phases, is also a likely solution. The structure map with contrast reversed shows distinct peak-like features near the cation positions within the framework. The potential near the pore structure exhibits a strong oscillation. This may arise from lack of physical constraint in an open framework structure; anisotropic Debye-Waller factors can be larger than the isotropic factors by a factor of two for the atoms bounding the large pores, therefore loosely-constrained atoms within the pore structure would contribute some scattering from within the pore.

While we have used precession to demonstrate something very close to the true structure of Mordenite, the path to its determination was less straightforward than in the previous examples in this chapter. At this time, one might argue that precession is not accurate enough to ensure reliable determination of
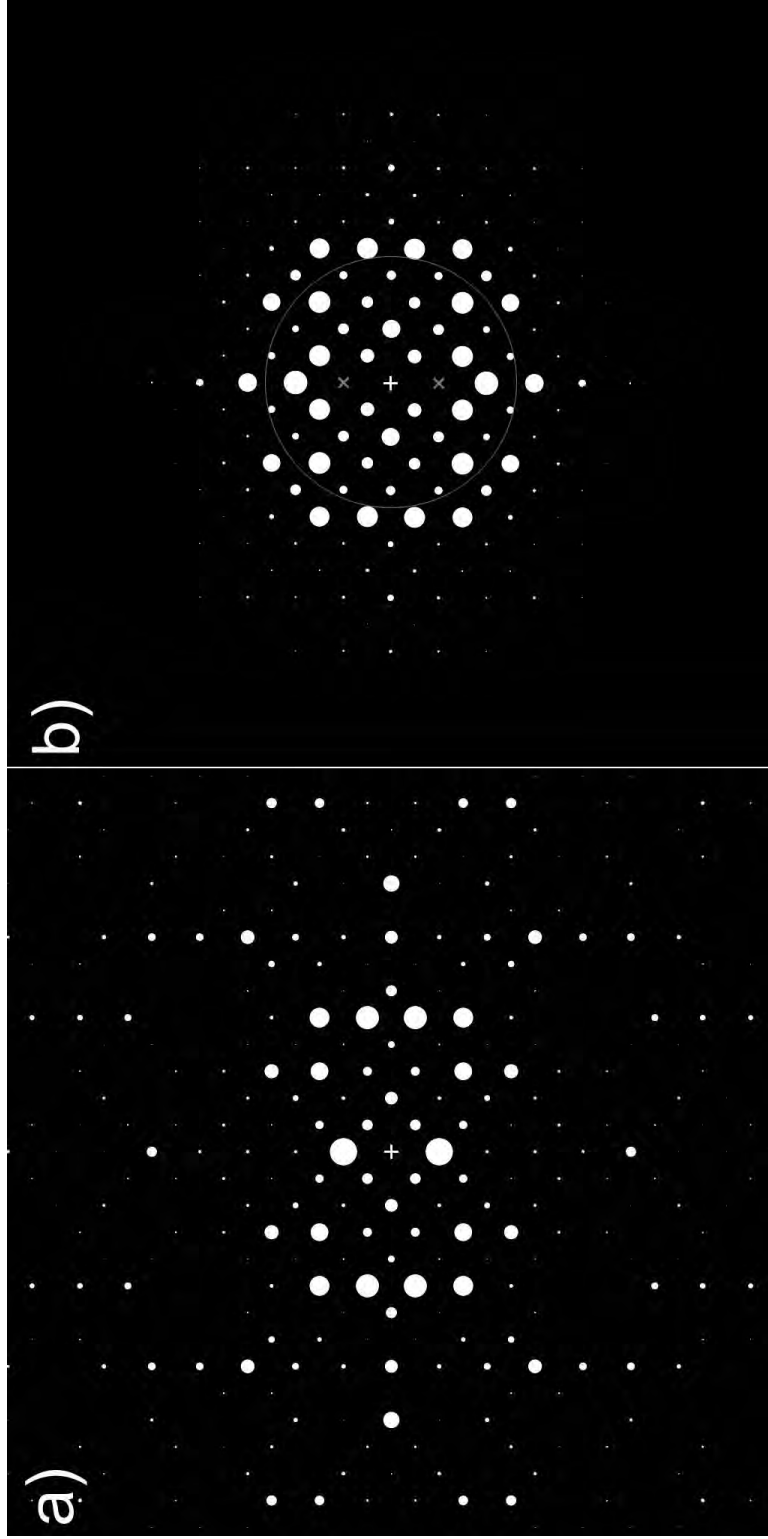
Figure 5.9. (a) Kinematical diffraction pattern for Mordenite [001] zone axis. (b) The precession pattern for the same zone ($\phi = 40$ mrad). The spatial frequency $g = 0.25$ is indicated the ring overlay.
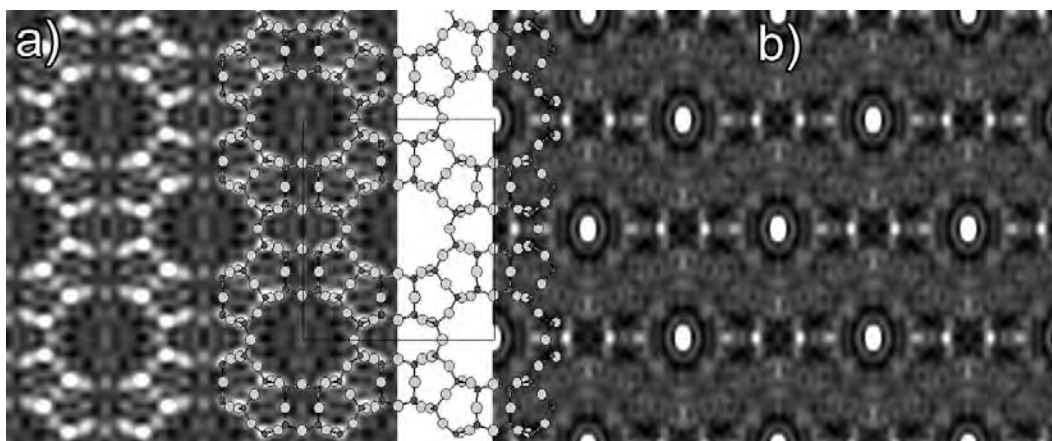
Figure 5.10.   (a) Structure map from direct methods on Mordenite using kinematical amplitudes to 1 Å^{-1} with no additional phases. The cation locations are poinpointed but the structure map has many spurious Gibbs oscillations due insufficient sampling of spatial frequencies. (b) Preliminary PED direct methods solution using amplitudes with direct methods (no filtering). Considerable intensity is put into the pore centers where no atoms should exist, and spurious oscillations occur throughout the denser regions of the structure. The true structure is overlaid on top of both solution maps for reference; light atoms represent Al/Si and dark atoms represent O.
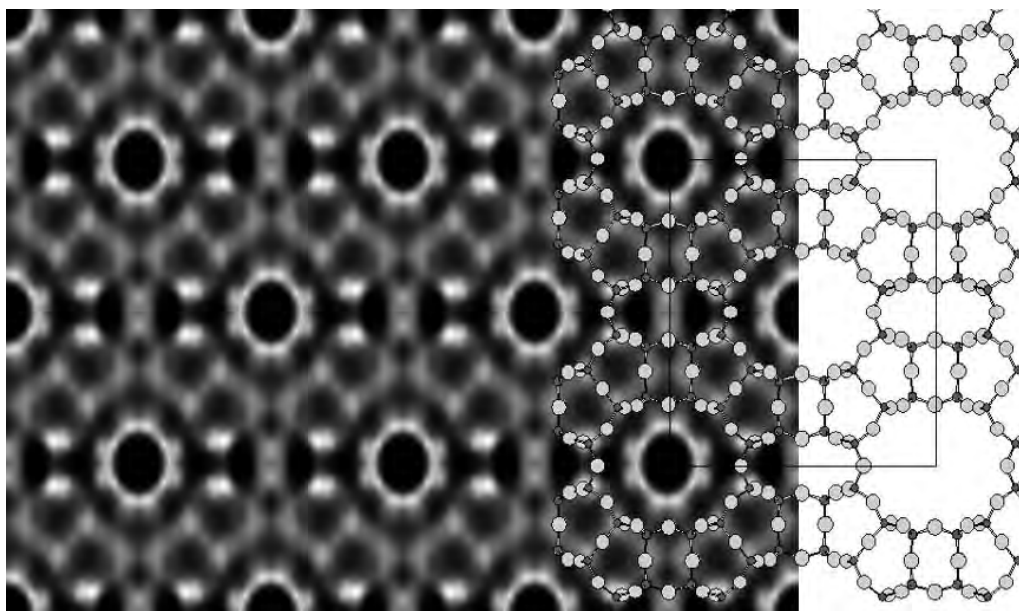

Figure 5.11.   Direct methods potential map of Mordenite generated using high-pass filtered intensities. Peaks occur near cation locations within the framework.

weakly scattering loose framework structures from the *ab initio* structure solution standpoint. In a case such as this, high-resolution phases should be used with PED intensities to constrain the solutions.

5.5. Conclusion

This chapter has demonstrated procedures for generating starting structure maps. The materials systems investigated in this chapter possess differing compositions and structures, and have demonstrated some of the advantages as well as disadvantages of precession from a practical standpoint. Generally, the structure maps from direct methods on PED data give realistic positions and features as long as the projection constraint is reasonably satisfied. When precession data is used, the direct methods solutions list always contain maps that are sparsely populated with well-defined discrete peaks. The correct solution can be readily filtered out from these. Perhaps the most remarkable feature is that realistic maps — of which GITO was one example that produced essentially exact atoms positions — were generated without the use of *any* fixed phases.

It is important to note that these are all known structures and some influence on how the studies were carried out was influenced by *a priori* knowledge. Additionally, the types of structures shown here do not represent the huge variety of possible problems. However, the examples do show that the true solution is indeed contained within the list of potential solutions generated by direct methods, and the amount of work necessary to generate a good starting structure for refinement is considerably diminished compared to conventional electron crystallography.